Cold Spray Deposition of Inconel 718 in Comparison with Atmospheric Plasma Spray Deposition

Zheng ZHANG,[a] *Debbie SENG Hwee Leng,*[a] *Ming LIN,*[a] *Siew Lang TEO,*[a] *Tzee Luai MENG,*[a] *Coryl Jing Jun LEE,*[a] *Zhi-Qian ZHANG,*[b] *Te BA,*[b] *Junyan GUO,*[b] *Kannan SUNDARAVADIVELU,*[b] *Poh Koon AW,*[c*] *and Jisheng PAN* [a#]

[a] Institute of Materials Research and Engineering (IMRE), A*STAR (Agency for Science, Technology and Research), #08-03, 2 Fusionopolis Way, Innovis, 138634, Singapore.

[b] Institute of High Performance Computing (IHPC), A*STAR (Agency for Science, Technology and Research), 1 Fusionopolis Way, Connexis, 138632, Singapore.

[c] Singapore Institute of Manufacturing Technology (SIMTech), A*STAR (Agency for Science, Technology and Research), #08-03, 2 Fusionopolis Way, Innovis, 138634, Singapore.

Corresponding Authors:

*Tel.: +65-64197404

*Fax: +65-68720785

*E-mail address: pkaw@simtech.a-star.edu.sg

#Tel.: +65-63194919

#Fax: +65-68720785

#E-mail address: js-pan@imre.a-star.edu.sg

ABSTRACT

Inconel 718 is a Ni-based superalloy which has been widely used in aerospace industry. Repairing of Inconel 718 components has been usually carried out using atmospheric plasma spray (APS) and high velocity oxy fuel (HVOF) spray techniques. Cold spray (CS) is a relatively new thermal spray technique, which relies more on powders' kinetic energy and less on their thermal energy to impact powders onto the substrate, where the powders undergo severe plastic deformation and subsequently adhere to the substrate surface as coatings. In this work, high pressure CS using dry N_2 as propellant gas has been deployed to deposit Inconel 718 powders as thick coatings for structural restoration application. The coating's surface morphology, cross-section microstructure, crystallinity, residual stress and mechanical properties were subsequently characterized and compared with the Inconel 718 coating deposited by APS in order to elaborate the unique features of the Inconel 718 coatings deposited by both spray techniques.

Keywords: Inconel 718; Cold spray; Atmospheric plasma spray; Thermal spray; Coatings.

I. Introduction

Superalloys are a family of metallic alloys which can maintain mechanical strength, chemical composition and structural integrity at elevated temperatures under high stress and in oxidizing or corrosive environment [1-3]. Based on the dominant metal present in the alloy, superalloys can be classified as iron-based, cobalt-based and nickel-based superalloys. Among these three superalloys, nickel-based superalloy has exceptional combination of high temperature strength and toughness. Hence, they have been widely used in gas turbines for aircrafts, power-generation and marine propulsion [1-3].

Inconel 718 alloy is the most widely used nickel-based superalloy in aircraft industry due to its good tensile, fatigue, creep and rupture strength together with ease to fabricate. It can be applied in a wide operation temperature window from -253 ^{o}C up to 650 °C for a long service life [2, 3]. It accounts for more than 30% weight percentage of a modern aircraft engine [2] and has also been used for fasteners, liquid fueled rockets, land-based gas turbine engines and cryogenic tankage. Cr and Fe are the two main alloying elements with other minor aging constituents including Nb, Mo, Ti and Al. In the mill annealed or stress relieved condition, Inconel 718 is dominated with a relatively soft face-center-cubic γ-matrix (Ni-Cr-Fe) phase and hence can be machined, formed or welded easily. The components after fabrication usually undergo solution heat treatment (927 to 1066 ^{o}C) with or without further precipitation aging (593 to 816°C) so that the hardening secondary phases (γ′ (Ni_3(Al,Ti) and γ′′ (Ni_3Nb)) can precipitate and strengthen the alloy to achieve its full strength.

Due to their harsh operation environment such as high temperature (~ 650^{o}C) and under high loading, these gas turbine components made of Inconel 718 often suffered from wear and tear after long service duration. Instead of scrapping the worn-out components and replacing them with

new parts, it is of considerable commercial value to restore the structural integrity of the components through repairing, especially when the lead times for new replacement parts are unacceptable or when the replacement parts are obsolete and unavailable. Different repairing techniques, such as laser metal deposition (or laser additive deposition) [4] and thermal spray [5-20], have been proposed. Laser metal deposition has advantage of small spot size, precise deposition, capability to deposit graded materials with low distortion and small heat affected zone [4, 21]. Their small laser spot size offers high dimensional accuracy, but results in a lower buildup rate. On the other hand, thermal spray techniques offer higher coating buildup rates and has been widely used in maintenance, repair and overhaul (MRO) of components in aerospace industry.

Traditionally, the thermal spray techniques utilize thermal energy to melt the Inconel 718 powders in a plasma [5] or flame [6-8] while these powders are propelled towards the substrates. Thereafter, the molten powders impact the substrate, form splats, solidify and cool down as Inconel 718 coatings. A few hundred microns up to 2.7 mm thick coatings have been deposited using atmospheric plasma spray (APS) [5] and high velocity oxy-fuel (HVOF) spray [6-8]. Both techniques tend to result in high porosity: 2.2 - 3.2% for APS [5] and 0.5 - 2.2 for HVOF [6]. In addition, it was found that the coating's adhesion strength (72.2 - 124.7 MPa) by HVOF was positively related with the powder velocity and powder temperature [6, 7]. Higher powder velocity also led to lower porosity but higher oxide content in the coating [6]. Inconel 718 coating's Young's modulus was higher when measured in cross-section than at the surface, with both of them lower than that of the Inconel 718 coupon [8].

Recently, another thermal spray technique, cold spray (CS), has been demonstrated capable to deposit thick Inconel 718 coatings as well. CS utilizes more of metallic powders' kinetic energy and less on their thermal energies to form coatings [22]. In CS, micron-sized metallic powders are propelled by a pressurized inert gas (up to ~ 5 MPa), which can be N_2, He or a mixture of both and

pre-heated to a maximum temperature of 1100 ^{o}C. The powders are only softened but not melted by the heated gas. The hot powder-gas mixture goes through a DeLaval nozzle with a converging-diverging cross-section. Subsequently, powders can reach supersonic velocities (300 to 1200 m/s) upon impacting the substrates with the appropriate combination of gas type, gas pressure, gas temperature, powder size and stand-off distance. If the powders' velocities are above a critical velocity (V_{cr}), the conversion of kinetic energy of the hot powders into thermal and strain energy upon impact would cause them to undergo severe localized plastic deformation and adiabatic shear instability at the powder-substrate interface[22, 23]. Consequently, the surface oxide scales at the contact point are broken and removed, causing certain degree of intermixing at the powder/substrate interface and the formation of a fresh metallurgical bonding. As a result, the impacting powders adhere to the substrate, leading to first layer of metal deposit. Dense and thick metallic coatings with low porosity can be produced with repeated spray. If the impact velocity is lower than the V_{cr}, the powder will bounce off and not stick to the substrate. If the impact velocity is too high ($> 2 \times V_{cr}$), the powder will erode the substrate instead of sticking to the substrate [23]. The V_{cr} can be affected by powder materials, powder size, powder temperature and substrate materials.

After the successful demonstration of cold spray for depositing thick soft metallic coatings including Cu [24, 25], Al [26-28] and Sn [29], cold spray has been employed to deposit hard metals including pure Ti [30, 31], Ti-6Al-4V alloy [31, 32], pure Ni [33, 34] and Ni alloys (such as Inconel 718 and Inconel 738) [9-18]. In the recent three years, there have been considerable efforts to deposit Inconel 718 powders using high pressure CS and thick (3.2 mm [16]) dense Inconel 718 coatings with porosity less than 2.5% have been obtained [9, 11-13, 15]. Although the as-deposited Inconel 718 coatings were brittle [13], they had much higher hardness [12, 20] and better wear resistance [20] compared to those of the bulk Inconel 718 coupon. Through furnace annealing [9,

10, 13-15, 17, 19], local induction heat treatment [19] or hot-isostatic-pressing (HIP) [15], the tensile strength [10, 14] and adhesion strength [12, 17] of the Inconel 718 coatings can be considerably improved while their porosity [9] and hardness [9, 13-15] were reduced.

The research so far has investigated the effects of different process parameters and subsequent heat treatment on the microstructural and mechanical properties of the Inconel 718 coatings deposited by CS. As atmospheric plasma spray (APS) has been widely used in maintenance, repair and overhaul (MRO) of airspace industry, it would be worthwhile to compare the Inconel 718 coatings deposited by APS with those by CS in order to understand their unique characteristics, strength and weakness for better deployment of each technique as repairing or additive manufacturing options. However, the researches so far have been focusing on each of them without a comprehensive comparison between these two techniques. Therefore, in this work, we have conducted a comparative study on Inconel 718 coatings deposited using both APS and CS. The resultant coatings' phase, morphology, porosity, microstructure, hardness and tensile strength are compared to better illustrate the characteristics of each technique.

II. Experimental methods

Inconel 718 powders manufactured by Plasma Giken Co. Ptd (PG-AMP-1070) and Oerlikon Metco (Amdry 718) were used for cold spray (CS) and atmospheric plasma spray (APS) deposition, respectively. They were subsequently named as PG 718 and Amdry 718 for brevity. Powders' size distribution was analyzed using Malvern Mastersizer 2000 particle size analyzer with 3000 rpm stirring speed and a refractive index of 1.9648 after dispersing powders in ultra-pure water. Commercial Inconel 718 coupons with average Vickers hardness of 245.8 HV_{200g} were used as the substrate. CS and APS deposition were carried out using Plasma Giken cold spray PCS-1000 system and Oerlikon Metco UniCoatPro plasma spray system, respectively. The optimized spray

parameters were listed in Table 1.

Table 1 Process parameters used in cold spray and atmospheric plasma spray*

Cold Spray (CS)		Atmospheric Plasma Spray (APS)	
N_2 pressure (MPa)	4.0	Current (A)	470 - 500
Gas temperature (°C)	800	Voltage (V)	70 - 80
Standoff distance (mm)	30	Standoff distance (mm)	100 - 125
Robot scan speed (mm/s)	500	Gun travel speed (mm/s)	1250
Powder feedrate (g/min)	23	Powder flowrate (g/min)	40 - 50
Number of pass	5	No of passes	20
Grit-blasting	No	Grit-blasting	Yes
		Ar flow rate (NLPM)	40 - 45
		H_2 flow rate (NLPM)	7 - 10
		Carrier gas (Ar) flow rate (NLPM)	2.8 - 3.5
		Powder inject size (mm)	ϕ 1.5
		Compressed air jet (bar)	2

(*: most parameters in APS were listed as a range instead of finalized values due to confidential agreement with the equipment supplier.)

The coatings' morphology and composition were analyzed by JEOL field emission scanning electron microscope (FE-SEM 7600F) equipped with Oxford Instruments X-Max 50 energy dispersive spectroscopy (EDS, Aztec Synergy System). The grain morphology and orientations from the cross-section surface of the coatings were examined by JEOL IT500HR FE-SEM, equipped with Oxford Instruments Symmetry EBSD detector, using 20 kV electron accelerating voltage and a scanning step size from 0.2 to 0.5 μm. The surface residual stress was measured using the $\sin^2\psi$ method with Cr Kα X-ray without filter in Stresstech Xstress G3 X-ray stress measurement, and the shift of Ni (311) planes ($2\theta = 155 \pm 2$ °) were detected. The cross-section surface of Inconel 718 coatings was mechanically polished using SiC grinding paper down to grit 4000, followed by MD Mol (3 μm) and MD NaP OPS (0.3 μm) final polishing. Images of the cross-section were taken by Olympus BX53M optical microscope, and the porosity inside the coatings was subsequently calculated using ImageJ software based on these images. The crystalline structures of the coatings were examined using Bruker D8 Advance X-ray diffraction

with Cu Kα X-ray (λ = 1.54 Å) at a voltage of 40 kV and a current of 40 mA. Coating's hardness and Young's modulus were evaluated by Agilent G200 nano-indentation using a continuous stiffness measurement (CSM) technique with a Berkovich indenter (three-faced pyramid diamond). During the indentation test, the indenter was pressed into the cross-section of the coating and substrate with a constant strain rate (0.05 s^{-1}) to 1000 nm deep. Marco-hardness measurement was carried out using Innovatest Falcon 5000 hardness tester with a Vickers indenter. The bond strength of coatings was evaluated by pulling test using the Instron double column universal mechanical tester 5569. Two types of glue, Master Bond EP15ND-2 and HTK Ultrabond 100, have been separately applied to ensure that the glue has a higher adhesion strength than that of the coatings.

FEI Helios Nanolab 450S dual beam focused ion beam (FIB) system has been used to prepare a cross-section thin slice from the polished top surface of the Inconel 718 coating deposited by CS for transmission electron microscopy (TEM) characterization in a JEOL-2100 TEM operating at 200 kV. The JEOL 2100 is equipped with a double tilt low-background TEM holder, an Oxford EDS detector, a DigiSTAR Precession electron diffraction system and Nanomegas ASTAR phase and orientation mapping system. The crystallographic orientation mapping was obtained through scanning the area of interest at Nano-beam diffraction mode with step size of 10 nm and actual beam size of ~ 6 nm using a 10 μm condensed aperture. The electron diffraction patterns were indexed by comparison with standard FCC NiCr (space group of Fm-3m with a=3.591Å). The final process maps were visualized and analyzed using HKL Channel 5 (Oxford Instruments) software.

III. Results

The as-received powders' morphology and size distribution are shown in Fig. 1. It can be seen from the SEM images that both powders were spherical in shape (Fig. 1(a, a′)). While PG

718 powders for cold spray (CS) were mainly comprised of well-separated spheres, small powders with size of 8 ~18 µm were frequently attached to the main powders as satellites in Amdry 718 powders for atmospheric plasma spray (APS). The D_{10}, D_{50} and D_{90} powder diameters for PG 718 powders were 10.1, 18.1 & 31.0 µm, while those for Amdry 718 powders were 50.0, 71.6 & 102.7 µm, respectively, as determined from particle size analyzer (Fig. 1(b, b′)).

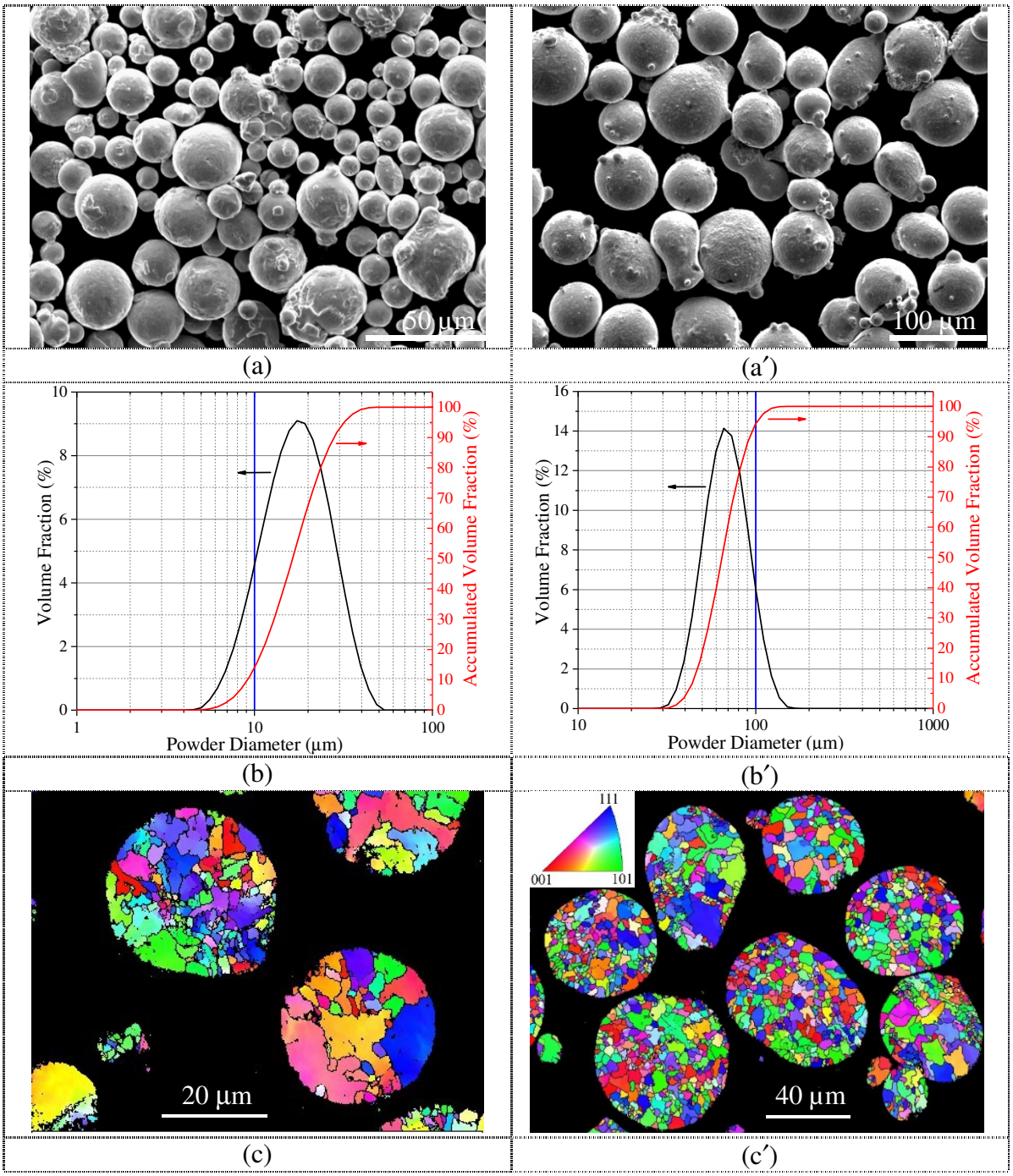

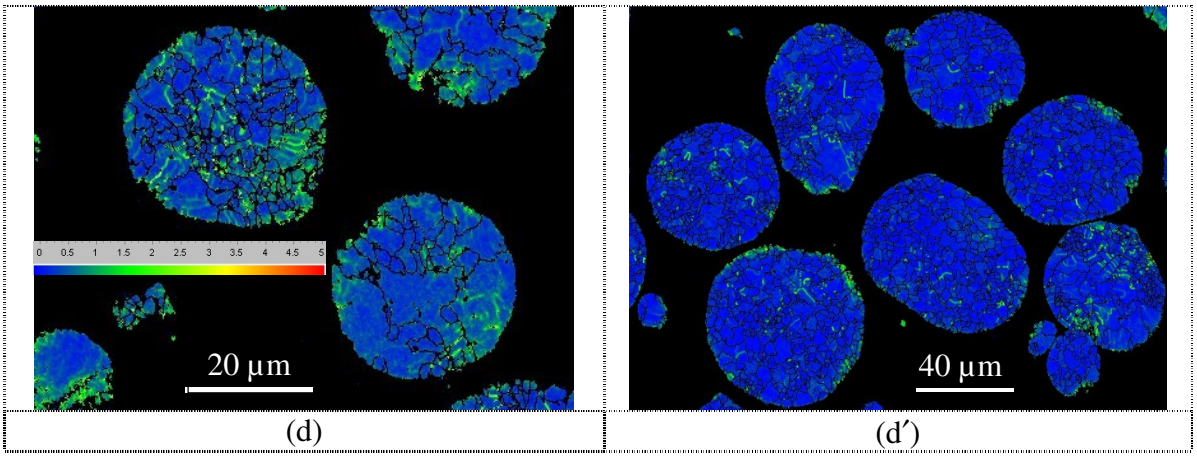

Fig. 1 (a, a′) SEM images of powder morphology, (b, b′) powder size distribution, (c, c′) EBSD inverse pole figure map in z direction and (d, d′) kernel average misorientation (KAM) maps of (a, b, c, d) PG 718 powders and (a′, b′, c′, d′) Amdry 718 powders. The grain orientations and KAM map were colored following the triangular legend in the inset of (c′) and color scheme in the inset of (d), respectively.

The inverse pole figure (IPF) maps of NiCr γ-phase in the z-direction (out-of-plane) from electron backscattering diffraction (EBSD) analysis provide the crystallographic orientations perpendicular to the analysis surface from the cross-section of the powders (Fig. 1(c, c)′). The high angle grain boundaries (HAB), defined here as misorientations greater than 10°, are highlighted as black lines. IPF maps show that both powders were dominated with mixture of large and small grains randomly orientated within each powder. The grain diameter determined from EBSD for PG 718 and Amdry 718 ranges from 1.0 ~ 12.6 µm and 1.1 ~ 17.9 µm, respectively. Although D_{50} of PG 718 powder size was about one fourth that of Amdry 718, the average grain diameters for both powders were comparable at ~ 3 µm. Kernel average misorientation (KAM) maps were generated to evaluate the extent of the local misorientations within each powder. The KAM value for each pixel was taken as the averaged misorientation value between itself and its 8 nearest neighboring pixels. Misorientations greater than sub-grain angle of 5° were defined as threshold and were excluded in the calculation. The KAM maps were colored according to the color scheme in the legend (as inset in Fig. 1(d)), where higher local misoriented (> 2°) and the lower local

misoriented regions (< 1°) were colored in green and blue, respectively. The grain boundaries were defined for misorientations greater than 10°, same as the definition of HAB for IPF. It can be seen from KAM map in Fig. 1 (d, d′) that the bulk of both Inconel 718 powders showed low local misorientations (as represented by blue color), despite that they were of different sizes and manufactured by different suppliers.

Following the spray parameters listed in Table 1, the resultant surface morphology of Inconel 718 coatings can be found in Fig. 2. Both coatings appeared rough due to the nature of powder-based spray technology. The average roughness (R_a) was 13.4 ± 1.7 and 17.0 ± 3.6 μm, respectively, for Inconel 718 coatings by CS and APS. The entire surface of Inconel 718 coating by CS was decorated with slightly deformed spherical powders with upper half intact while the bottom half embedded in the coating (Fig. 2(a &b)). Such surface morphology suggests that the powders were not molten during the spray process thanks to the relatively low temperature process, and has been similarly observed in other Inconel 718 coatings deposited by CS [9, 10, 18-20]. However, surface of Inconel 718 coating by APS was covered by fragmented fine particles with very smooth surfaces in between (Fig. 2(b′)), characteristics of molten powders and indication of the high temperature that the powders went through. The initial spherical shape of the powders was no longer discernible after deposition, despite that their sizes were much larger than those of the PG 718 powders. The surface composition of the Inconel 718 coating by CS does not differ significantly from the composition of the starting PG 718 powders (Fig. 2(c)). However, for the Inconel 718 coating by APS, there was a clear increase in O wt% from 0.7 wt% in the starting Amdry 718 powder to 10.0 wt% in the APS Inconel 718 coating, and a concurrent decrease in Ni & Fe wt%. The higher O wt% in the coating was due to the high temperature plasma the Amdry 718 powders flied through, and indicates a higher degree of oxidation in the Inconel 718 coating by APS.

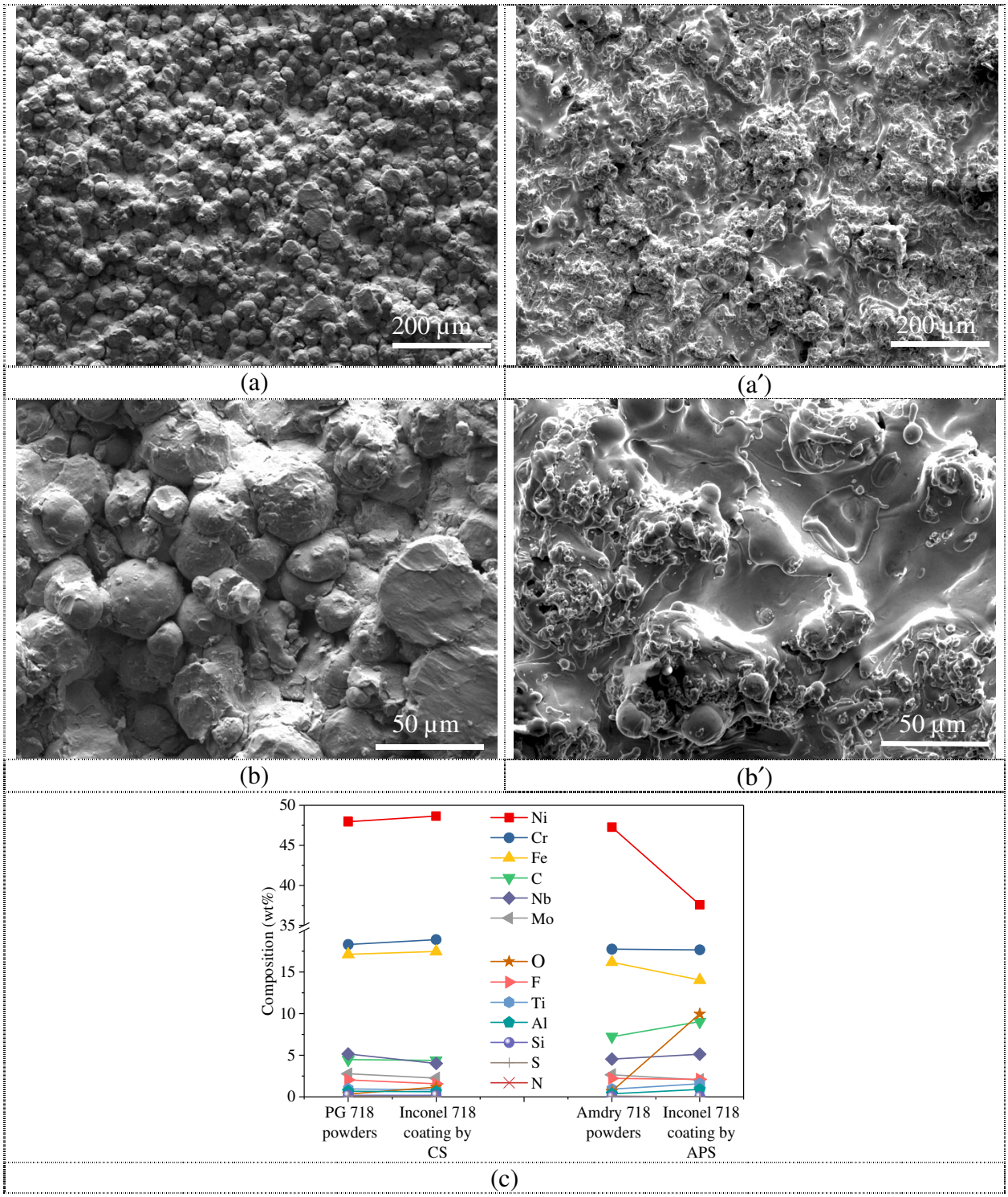

Fig. 2 SEM images of surface morphology from as-deposited Inconel 718 coatings by (a & b) CS and (a´& b´) APS. (b & b´) shows a higher magnification from the area in (a & a´), respectively. (c) shows the composition in weight percentage (wt%) from both coatings and the starting powders.

The XRD patterns show that the dominant phase present in both Inconel 718 coatings

deposited by both CS and APS was face centered cubic NiCr γ-phase (PDF card: 01-071-7594), similar to the patterns from the as-received PG and Amdry 718 powders. CS is known to preserve the original powders' crystallinity in the coating [15, 19, 20], while the optimized APS has also been able to maintain the original powder phase [5]. X-ray stress measurement revealed a compressive residual stress of -30.5 ± 12.5 MPa in the Inconel 718 coating by CS, but a tensile residual stress of 254.4 ± 33.3 MPa in the Inconel 718 coating by APS.

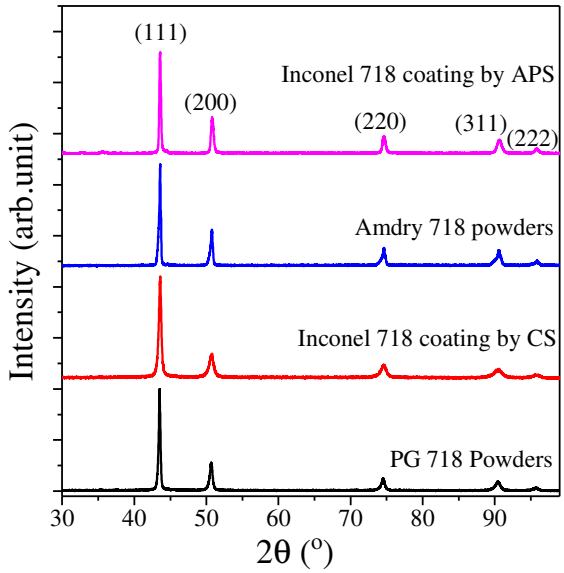

Fig. 3 XRD patterns of the as-sprayed Inconel 718 coatings by CS and APS. The XRD patterns from as-received PG 718 powders and Amdry 718 powders were also included for comparison.

The cross-sectional microstructures of the coatings at 100 times magnification under optical microscope are shown in Fig. 4. The thickness of Inconel 718 coatings by CS and APS were measured to be 683.9 and 240.4 μm, respectively, with the coating by CS clearly denser than the coating by APS. Besides pores in the coatings, the boundaries between powders can only be vaguely identified in the coating by CS (Fig. 4(a)). On the contrary, both pores and powder boundaries (i.e., black lines between the melt lamellars) can be seen clearly in Inconel 718 coating by APS (Fig. 4(a′)). The vague powder boundaries and the lamellar cross-section are the typical

features of coatings by CS [9-14, 16, 17, 20, 35] and APS [5], respectively. The porosity was calculated to be about 0.2 - 0.5 % and 0.8 - 1.5 % in Inconel 718 coatings by CS and APS, respectively, based on a series of optical micrographs from 50 to 200 times magnification. It should be noted that under the optimized recipes for both CS and APS listed in Table 1, the porosities in both Inconel 718 coatings deposited by CS and APS were at the lower end of the reported porosities by CS (0.4 - 2.5%, [9, 11-13, 15]) and APS (2.2 - 3.2%, [5]) in the literature. The porosity was lower in the Inconel 718 coating deposited by CS than that by APS. Moreover, the interfaces between coating and substrates in both coatings were quite intimate. The straight interface in coating by CS (Fig. 4(a)) corresponds with absence of grit-blasting prior to deposition, while the undulated interface in the coating by APS was associated with the grit-blasting prior to deposition. Despite different interface roughness, no visible gaps between coating and substrate can be seen in both cases, indicating that the bond strengths in both coatings could be rather decent.

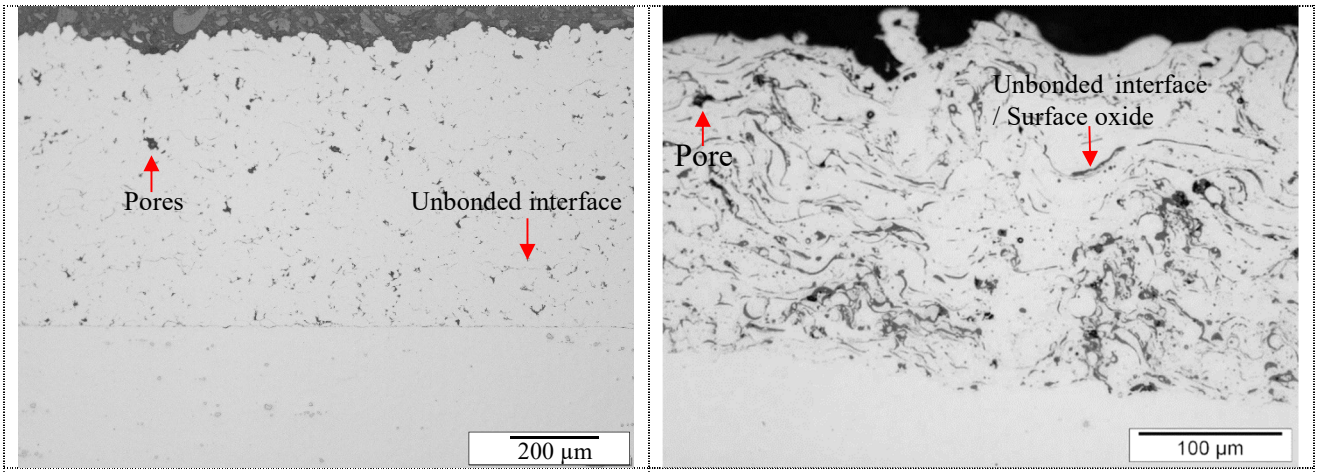

Fig. 4 Optical images from cross-section of the as-deposited Inconel 718 coatings by (a) CS and (a′) APS.

Detailed microstructures of both coatings as revealed under SEM and EBSD are shown in Fig. 5. From the forward scattered electron image, the pores inside the cold-sprayed coating can be seen clearly, while the powder boundaries can only be vaguely identified (Fig. 5(a)). The inverse

pole figure (IPF, Fig. 5(b)) map of the same area as Fig. 5(a) shows that the EBSD patterns from the Inconel 718 substrate were well indexed, while the EBSD patterns from the coating layer were poorly indexed with large areas un-indexed (shown in black). At the coating/substrate interface (marked with a white dotted box in Fig. 5(b)), there was a nearly continuous black strip, corresponding to the powders at the first pass of CS deposition. In addition, the grains at the top of the Inconel 718 substrate were shattered into small grains while the grains below this boxed area were largely intact. The KAM map shows that within the center of each powder (which was indexed under IPF), there were regions with high local misorientations as represented by green-yellow color (Fig. 5(c)). It is worth to note that the top 13.4 μm region of the substrate was also represented in green after CS deposition. In comparison, only the top 5.5 μm region had greater misorientations in the as-received Inconel 718 substrate prior to deposition (Fig. S1), mainly arising from the substrate supplier's grinding process. Hence, the forceful impact from Inconel 718 powders also contributed to thicker misoriented region in Inconel 718 substrate after CS deposition.

IPF map at a higher magnification with smaller step size (0.2 μm, Fig. 5(e)) focusing only on the coating (Fig. 5(d)) shows that the center of each powder was largely well indexed with large grain, while the periphery of each powder was comprised of very fine grains. However, the boundaries between powders cannot be indexed and appeared black. The KAM map (Fig. 5(f)) clearly shows that each powder was almost fully green, indicating highly misoriented regions inside each powder, except for occasional less misoriented region in the center (represented by blue). Compared with the original powders' spherical shape (Fig. 1(c)) and low misorientation state (Fig. 1(d)), the significant change in powder morphology, IPF and KAM maps after CS deposition clearly points out severe plastic deformation occur in every powder as well as in the top surface of the substrate after the CS deposition.

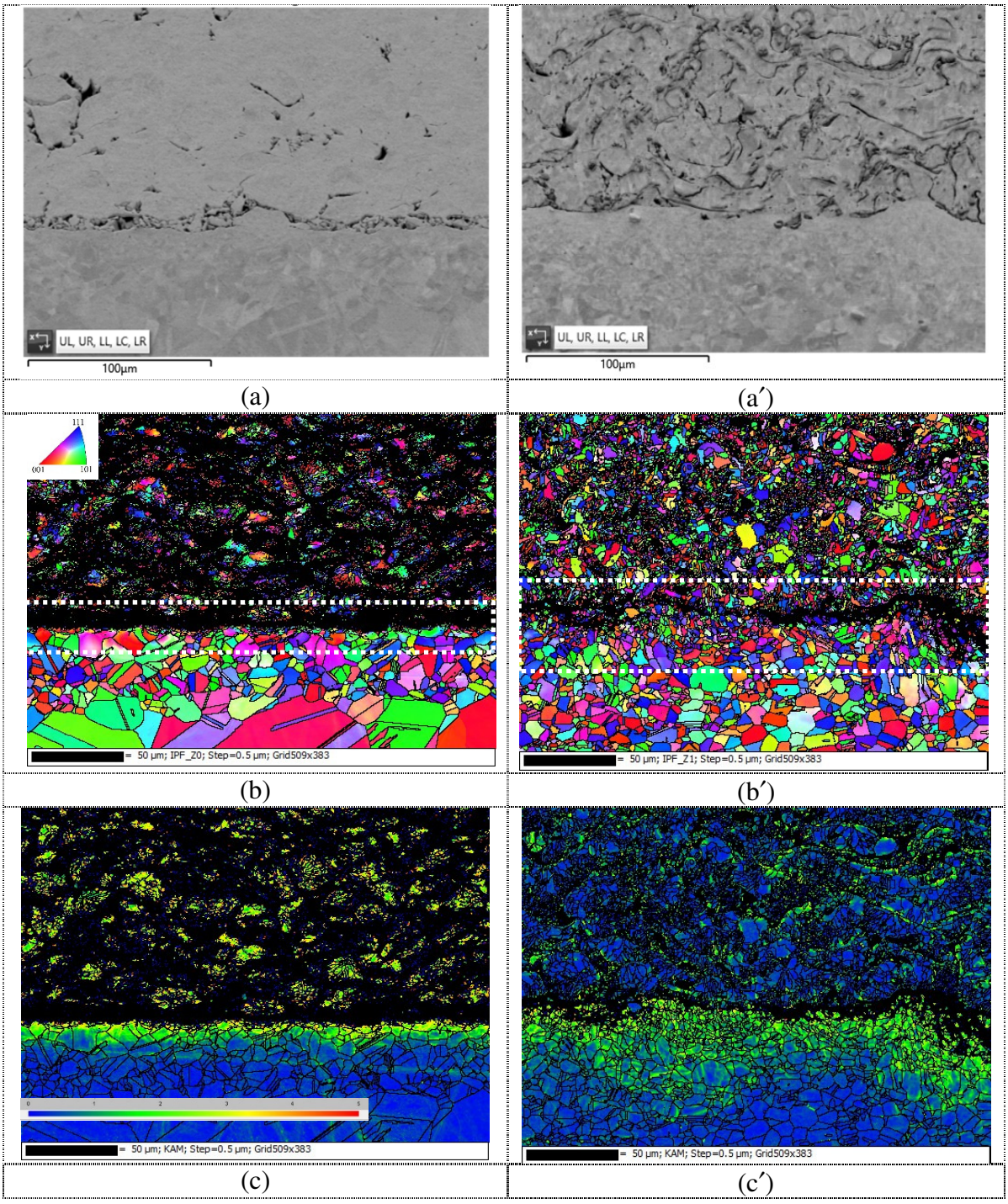
UL, UR, LL, LC, LR
100µm
UL, UR, LL, LC, LR
100µm
111
001
101
= 50 µm; IPF_Z0; Step=0.5 µm; Grid509x383
= 50 µm; IPF_Z1; Step=0.5 µm; Grid509x383
= 50 µm; KAM; Step=0.5 µm; Grid509x383
= 50 µm; KAM; Step=0.5 µm; Grid509x383

(a) (a′)

(b) (b′)

(c) (c′)

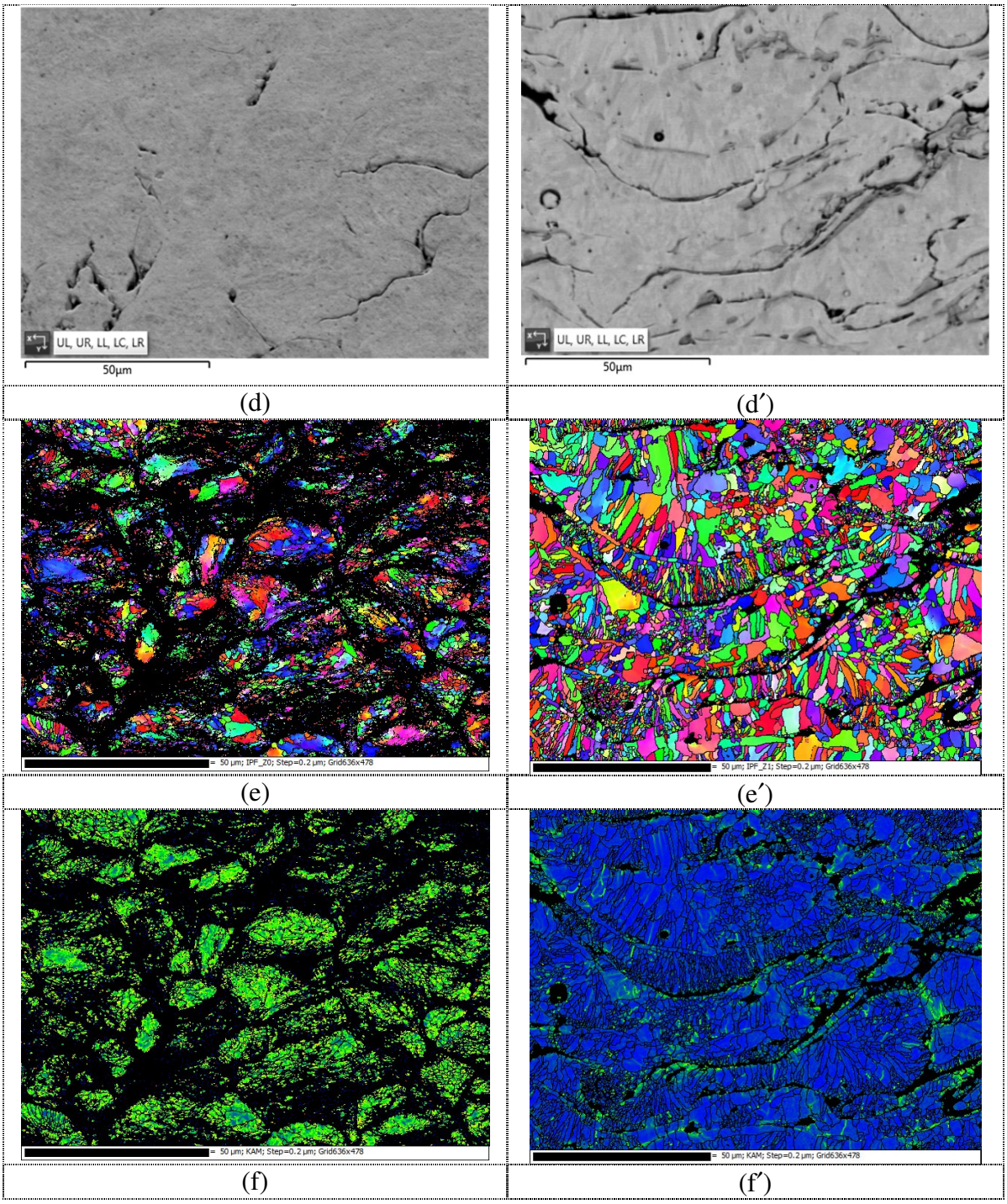

Fig. 5 (a, a′, d & d′) Forward scattered electron images (b, b′, e & e′) the inverse pole figures (IPF) maps and (c, c′, f & f′) kernel average misorientation (KAM) maps from Inconel 718 coatings by (a - f) CS and (a′ - f′) APS. (a - c′) show the overall image from both the coatings and substrates, while (d - f′) show the higher magnification from the coatings only.

The microstructure of the Inconel 718 coating by APS (Fig. 5(a′)) was quite different from

that of the CS coating. The IPF maps from both the coating and the substrate were well indexed as shown in Fig. 5(b′), except that there was a black strip along the coating/substrate interface (marked by white dotted box) and some black areas between the lamellars. The forward scattered electron image in Fig. 5(a′) clearly showed that the coating/substrate interface was intimate without gaps. Hence, the unindexed regions along the coating/substrate interface (Fig. 5(b′), which was similarly observed in Inconel 718 coating by CS in Fig. 5(b)) is likely due to presence of fine grains not resolved under EBSD scan, which will be elaborated more in Discussion session. Compared with the initial spherical Amdry 718 powders (Fig. 1(a′)), the molten powders have been squeezed by the impact force into two-dimensional lamellars. KAM map shows that the coating had very low misorientation (shown in blue, Fig. 5(c′)), except very limited green regions at the top of the 2D lamellars (Fig. 5(f′)). The highly misoriented region in the substrate (shown in green in Fig. 5(c′)) was clearly much thicker (ranging from 19 ~ 56 μm) compared to that in the Inconel 718 substrate used for CS deposition. It mainly arised from sand blasting prior to deposition together with the impact from molten Inconel 718 powders and the resultant softening of the substrate. In addition, the grains within these lamellars tended to align in the direction perpendicular to the contact surface (Fig. 5(e′)), which follows the temperature gradient when the molten powders rapidly cooled down and solidified upon impact on the substrate and lost the heat to underlying substrate and surrounding environment.

The microhardness of the Inconel 718 coating by CS was between 510.4 - 527.3 HV_{200g}, while the Inconel 718 coating by APS was between 227.5 - 252.2 HV_{200g}. The microhardness of the Inconel 718 coating by CS was in the same order as those reported earlier [11-13, 15] and about twice the microhardness of Inconel 718 substrate (245.0 - 247.8 HV_{200g}), while that of the coating by APS was slightly lower than the reported value of 300 ~ 350 HV_{50g} [5] but was close to the

Inconel 718 substrate's microhardness. Larger powders (50.0 ~ 102.7 μm) with a higher indentation force (200 g) compared to that in Ramesh's work (20 ~ 40 μm with 50 g, [5]) could lead to the lower hardness in our coating by APS. Even so, it can be seen that the Inconel 718 coating by CS was much harder than that by APS. Moreover, microhardness of coatings by both CS [12] and APS [5] was reported to increase with coating thickness.

The hardness and Young's modulus of the each coating and substrate were further evaluated using nano-indentation line scan across the coating into substrate. One of the typical line profiles is shown in Fig. 6, while the other line profiles can be found in Fig. S2 and S3. It can be seen that the hardness and Young's modulus line profiles follow each other's trend in both samples (Fig. 6). The cold-sprayed Inconel 718 coating's average hardness was 8.2 GPa, significantly higher than its substrate's average hardness value of 5.0 GPa (Fig. 6(a)). Out of the six line profiles we measured (Fig. S2), three of them showed a higher hardness at the first point above the substrate, e.g., the one at 11.6 GPa marked by dotted ellipse in Fig. 6(a). The enhanced high hardness near the surface was due to the impact between the first pass of layer with the underlying cold substrate, which work-hardens both the coating and substrate at the interface. The peening and work-hardening effects from the impacting powders on the substrate can be seen clearly by the gradual decrease of hardness in the substrate before it stabilized when the indentation points were moved away from the coating. During the subsequent pass of spraying, as both the preceding deposit and substrate were heated up from the initial impact and become warmer and softer, the consequent impact and work hardening were less significant and did not cause that much increase in the hardness of the coating. There were a few indentation points displaying lower hardness and Young's modulus (e.g., 2.8 and 103.2 GPa, respectively, marked by dotted rectangle in Fig. 6(a)) than the average hardness (8.2 GPa) and Young's modulus (210.2 GPa) of the coating, due to the presence of neighboring pores or gaps in the coating.

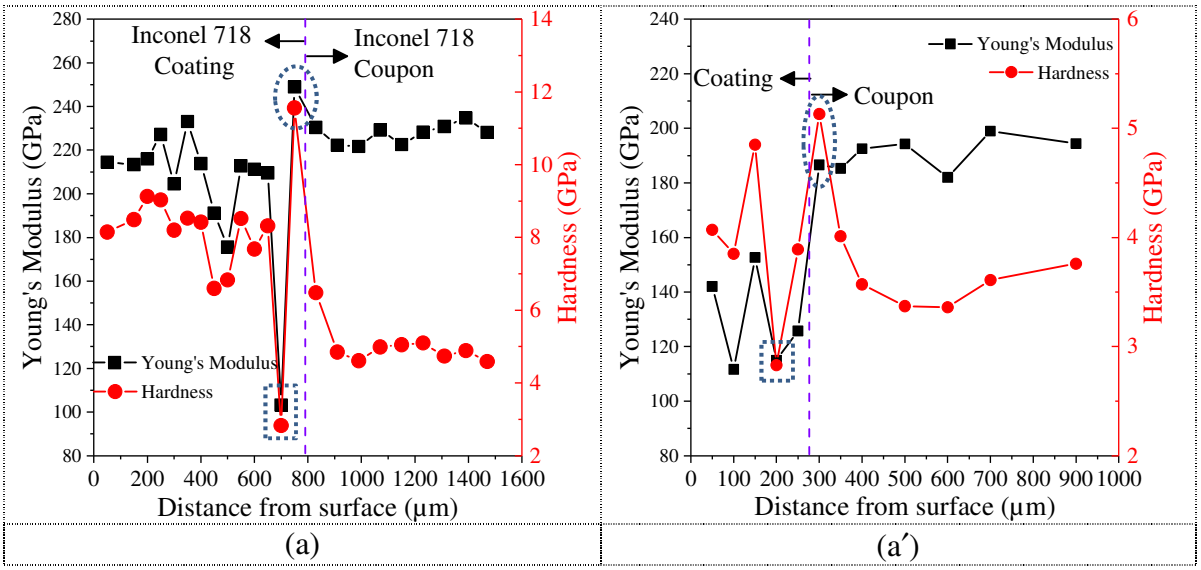

Fig. 6 Hardness and Young's modulus profile from Inconel 718 coatings by (a) CS and (b) APS on top of Inconel 718 substrates as measured by nano-indention line scan. The purple dotted vertical lines indicate the interfaces between coating (left) and the substrate (right).

The average hardness of the Inconel 718 coating by APS was only 3.9 GPa (Fig. 6(a′)), close to the average value from its substrate (3.8 GPa). Fluctuation in hardness and Young's modulus inside the Inconel 718 coating was be similarly observed due to the presence of porosity, surface oxides and the gaps (Fig. S3), which led to some indented points with lower hardness and Young's modulus (2.8 and 115.0 GPa, respectively, marked by dotted rectangle box in Fig. 6(a′)). The substrate had a maximum hardness (5.1 GPa, marked by dotted ellipse) near to its surface, before the hardness gradually decreased and stabilized when the indentation points were moved deeper into the substrate. Such enhancement in hardness was attributed to work hardening caused by the grit blasting prior to APS deposition, which also led to a thicker region with higher misorientation observed under KAM map (Fig. 5(c′)). The average value Young's modulus from coating was about 129.4 GPa, lower than the average Young's modulus of 190.6 GPa from the substrate. It is worth to note that the hardness results from nano-indentation matches well with microhardness test result of a much harder Inconel 718 coating by CS compared to that of coating

by APS and substrate.

For measurement of adhesion strength, specimens were prepared by spraying ~ 300 μm Inconel 718 coatings onto Inconel 718 rods with 24 mm diameter. The adhesion strength of the Inconel 718 coatings by CS and APS were determined to be 74.0 ± 12.1 and 76.4 ± 6.1 MPa, respectively, while the bond strengths of both pure glues were tested to be ~ 94.4 ± 16.1 MPa. The adhesion strength from coating by CS was at the higher end of the reported adhesion strength values from 17 to 77 MPa [12, 17], which decreased as the coating thickness increased [12]. Although the adhesion strength for Inconel 718 coating by APS is not available for comparison based on our best knowledge, the coating by HVOF has observed an adhesion strength between 72.2 and 124.7 MPa [6, 7], encompassing the adhesion strength in our Inconel 718 coatings by APS. From the fractured surface after tensile test, it can be seen that the failure occurred at the interface between coating and the glue for both coatings (Fig. 7). In Inconel 718 coating deposited by CS (Fig. 7(a)), about half of the coating was completely pulled off and broke from the rest of the coating. In Inconel 718 coating deposited by APS (Fig. 7(a′)), only a small fraction of the coating was stuck with the glue and pulled off from the initial coating. It suggests that the adhesion strength in the coating by APS was slightly better than that of the coating by CS.

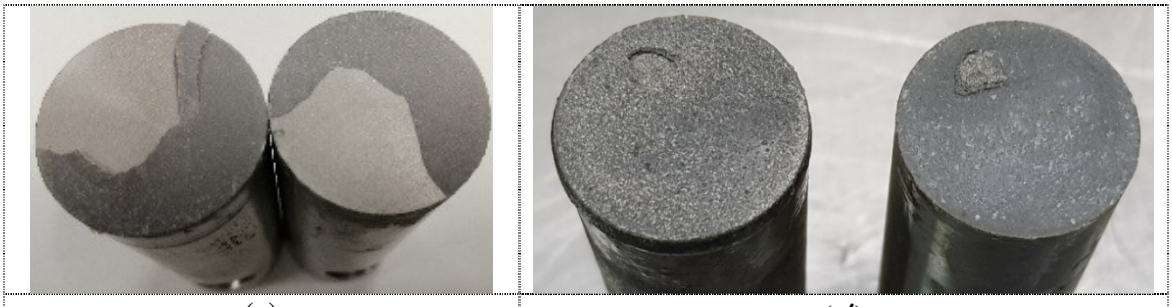

Fig. 7 Fractured surfaces from Inconel 718 coatings deposited by (a) CS and (a′) APS after the adhesion strength test.

In order to test the tensile strength of the as-deposited coatings, ~ 3.0 mm thick Inconel 718 coatings were deposited on carbon steel by APS and on bulk Inconel 718 by CS, respectively. The coatings were subsequently wire-cut from the substrates and prepared into flat dog-bones with the dimension described in Fig. 8. The solution heat-treated commercial Inconel 718 bulk coupon was fabricated into the same dog-bone geometry for benchmarking. The ultimate tensile strength of bulk Inconel 718 was 994.3 ± 3.5 MPa, while that of the Inconel 718 coatings by APS was 234.3 ± 10.3 MPa. The Inconel 718 coating by CS was very brittle and broke into two pieces at either of the holes during the tensile experimental setup before any valid readings were taken.

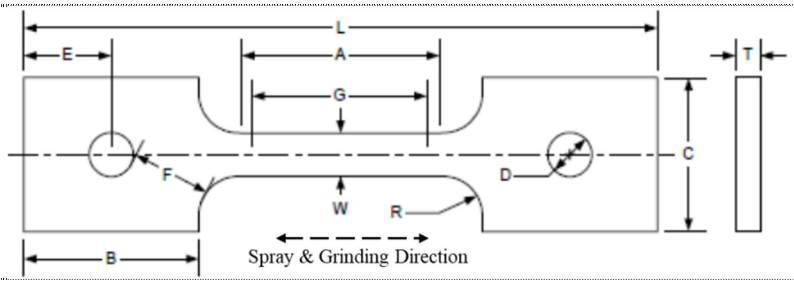

(a)

Unit	G	W	T	R	L	A	B	C	D	E
mm	16.26 ±0.05	4.06 ±0.05	1.50 ±0.025	3.96	68	24	18	15.24	6.00	9.00

(b)

Fig. 8 (a) Shape and (b) dimensions of the flat dog-bone sample for tensile test.

IV. Discussion

It is worth to note that the reported mean diameters of Inconel 718 powders used for cold spray (CS) are typically less than 35 μm [9-18], while they can be bigger for atmospheric plasma spray (APS). In CS, the powder with larger size can only reach a lower velocity with the same gas type and gas temperature [17, 22, 23]. As the Inconel 718 powders need to reach a critical velocity (V_{cr}) between 565 ~ 634 m/s at a temperature between 800 and 1000 ºC [15], the powders with smaller size (i.e., D_{50} = 18.1 μm, Fig. 1 (b)) were thus dominantly adopted for CS. In APS, the

temperature in the center of plasma is very high (12000 ~ 16000 ^{o}C [36]). Thus, Inconel 718 powders with higher powder size (D_{50} = 71.6 µm, Fig. 1 (b′)) were generally preferred to prevent severe oxidation and decomposition when powders fly through the extremely hot plasma even for a few milliseconds.

CS is a low temperature process (≤ 1100 ^{o}C) where the powders are not molten but only softened by the inert hot gas. Hence, one of its advantages is the ability to retain the original powders' composition and crystallinity. As a result, it can be seen that the cold-sprayed Inconel 718 coating still retained the spherical shape (Fig. 2(a)), composition (Fig. 2(c)) and crystalline phase (Fig. 3) of the starting powders. Using other sets of cold spray parameters where N_2 pressure and temperature were varied from 3 to 5 MPa and from 400 to 1000 ^{o}C, respectively, the resulting coatings' surface morphology, composition and crystalline phase also maintained those of the starting Inconel 718 powders (results not reported here).

In CS, the forceful impact of Inconel 718 powders with supersonic speed will introduce three main effects on the resulting coatings. Firstly, it induces severe plastic deformation and fragmentation at the contact surfaces, e.g., at the powder/substrate interface or at the interface with the preceding deposit. The conversion of kinetic energy into thermal energy upon powder impact causes the temperature at contact surfaces (i.e., powder/substrate interface or powder/powder boundaries) to surge above melting temperature [22, 23]. After heat was quickly dissipated to underlying substrate and surrounding environment, the molten interface quenched down, leading to very fine grain formation. Such fine grains with size less than 20 nm can be seen clearly under the bright field TEM image (Fig. 9(a)) as highlighted by the white dotted box, while the white dotted line marks the boundary between two particles, which was part of the fragmented powders. The grain size and corresponding crystallographic orientation of the NiCr γ-phase along the *x*, *y* and *z* direction can be further revealed by TEM crystallographic orientation map at nanometer

scale using the same sample (Fig. 9 (b-d)), where colors represent grain orientation as indicated inside the inset in Fig. 9(b). TEM crystallographic orientation mapping [37-39] is an extension of SEM-based EBSD to probe nanocrystalline's orientation which is beyond the resolution of traditional EBSD, such as for severely deformed metals [40]. As the grain size is far less than the step size used in EBSD (200 nm), the boundaries between powders thus were unresolved and appeared black under EBSD (Fig. 5(f)). Only the center of the powders, which have not gone through such dynamic recrystallization, can be indexed. Similar black regions along the powder boundaries have been observed in EBSD studies of other Inconel 718 coatings deposited by CS [11, 17, 33].

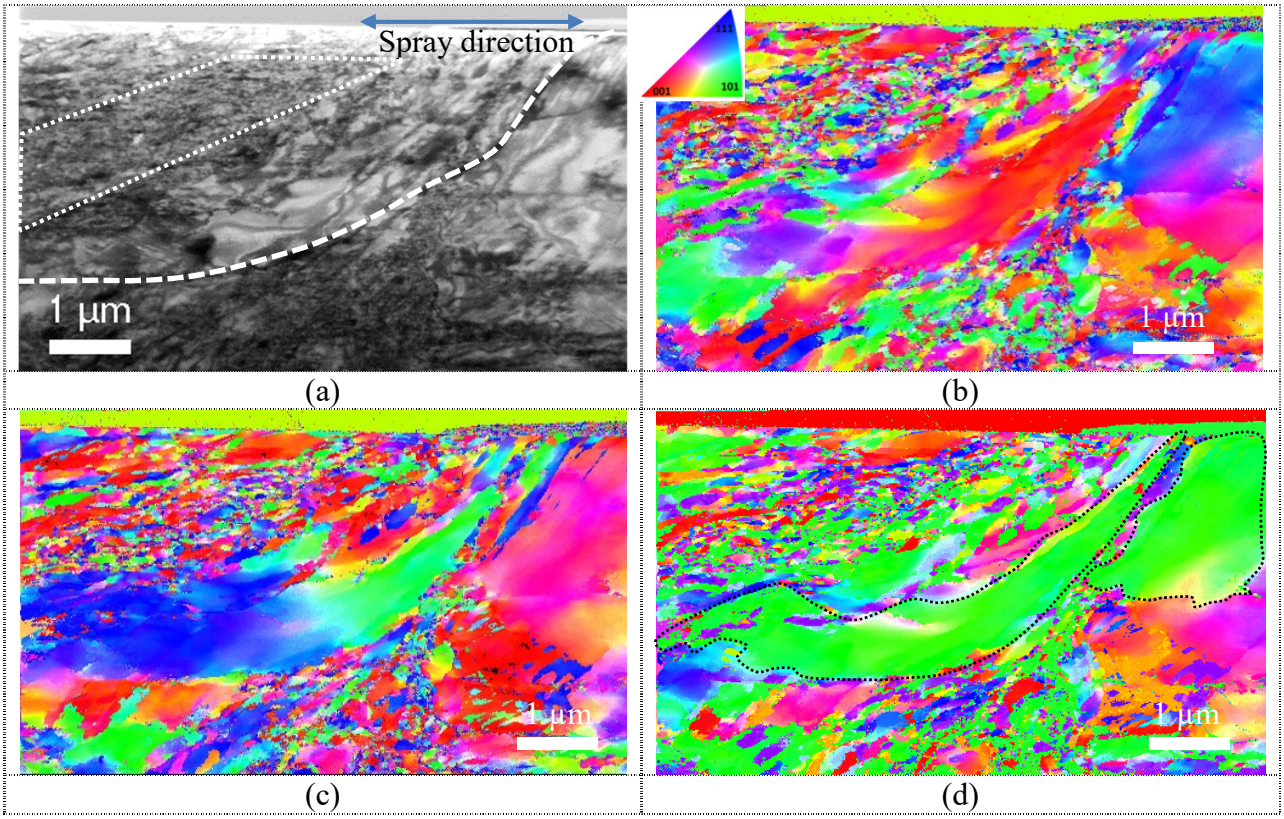

Fig. 9 (a) Bright field TEM image and TEM crystallographic orientation map of NiCr in (b) x, (c) y and (d) z directions from as-deposited Inconel 718 coating by CS (color code shown as inset in the top left corner of (b)).

Two large grains showing single orientation in *z* direction (represented in green) were circled out in Fig. 9(d) by two black dotted boxes along the interface between the impacted particles. By examining the crystallographic orientation in *x* and *y* directions (Fig. 9(b &c)), it can be seen that the green grain on the left in Fig. 9(d) was actually polycrystalline, comprising a few smaller grains with different orientations in *x* and *y* directions. By contrast, the green grain on the right in Fig. 9(d) was nearly single crystalline grain with uniform orientation in all three directions. Although fine grains (< 100 nm) were more frequently observed at the particle interfaces under TEM after CS deposition [19, 20], presence of large grains with 1 - 4 µm was reported as well in the pure Ni [33] and Cu [41] coatings deposited by CS, similar to the large grain in our case (Fig. 9(d)). Borchers *et al* [41] attributed the formation of such large dislocation-free grains to migration-type dynamic recrystallization, which is caused by a migration of pre-existing high angle grain boundaries and dislocations through the deforming microstructure and left a strain-free region thereafter [42]. Zou *et al* [33] drew a vivid schematic explaining such dislocation accumulation and annihilation process within a short time, leaving stress-free subgrains, which was further elaborated in [43].

Secondly, the forceful successive impacts by the powders also exercise peening and work hardening effects on the underlying substrate and the preceding layer, hence introducing a compressive residual stress in Inconel 718 coatings. The averaged residual stress calculated by measuring the bending curvature was - 245 MPa for a ~ 600 µm thick Inconel 718 coating [12]. The compressive residual stress resulted in very brittle Inconel 718 coating by CS which were fractured easily during wire-cutting or setting up the tensile test. Such compressive residual stress decreased with an increase in coating thickness [12, 17], likely due to stress relaxation when the underlying layer was heated up during the deposition of the subsequent layer. The relaxation and

reduction of compressive residual stress has been similarly observed when the Inconel 718 coatings were hot isostatic pressed at 1163 ^{o}C followed by solution and aging heat treatment [15]. The heat treatment also enhances the metallurgical bonding between powders which makes the brittle coating more ductile, evidenced by an enhancement of elongation from 0.48% to 2.94% after 4hr at 990 ^{o}C [14], from 0.5% to 14.5% after 1hr at 1200 ^{o}C [13], and from 0.23% to 24.7% after 1hr at 1250 ^{o}C [10]. The first two heat treatment were conducted in Ar atmosphere during heating and furnace-cooling [13, 14], while the third treatment was in 90%Ar/10%H_2 atmosphere[10]. An increase in the heat treatment temperature seems to foster better metallurgical bonding in the coatings and lead to better ductility.

Thirdly, the work-hardening caused by impact of the hard Inconel 718 powders led to a significantly higher hardness in the coating as compared to that of Inconel 718 substrate (Fig. 6(a)), which is similarly observed earlier [12, 15, 20]. The increased hardness led to a lower friction of coefficient and hence a lower wear rate (or better wear resistance) of as-deposited Inconel 718 coatings by CS compared to the Inconel 718 substrate [20]. Besides reducing the residual compressive stress, sintering the as-deposited Inconel 718 between 990 and 1250^{o}C also led to a reduction in the hardness [9, 14].

APS, on the other hand, is a high temperature deposition process (12000 ~ 16000 ^{o}C [36]) where the powders are usually molten after passing through the plasma. The resultant Inconel 718 coating thus displayed smooth area due to the solidification from the molten powders (Fig. 2(a′)) and had higher oxygen weight percentage due to susceptible oxidation by the surrounding air in high temperature (Fig. 2(c)). After optimizing the spray parameters, the resultant higher O wt% did not deteriorate and oxidize the coating adversely, as the crystallinity of the Inconel 718 coating was still well maintained (Fig. 3), although the high O wt% will have an impact on the service life

of actual repaired parts at high operation temperature. To prevent molten powder droplets from slipping away on the smooth surface, the substrate surfaces are usually grit-blasted to increase the roughness and hence enhance anchoring of the first layer of deposit via mechanical interlocking with the substrate. The subsequent deposit will follow the contour of the preceding deposit. The hindered contraction of the molten powders when they formed splats and cooled from the melting temperature to the underlying substrate's temperature thus resulted in the tensile residual stress in the coating by APS [44]. Such stress is also known as the intrinsic stress or quenching stress, and it has been reported to between 150 and 200 MPa for Inconel 718 coating by APS [44], close to the value we detected. Due to the high temperature deposition process, heat treatment was usually not performed in coatings by APS, and our as-deposited coating already possess decent ductility of 8.9%.

The solidification of the molten powders upon cooling down led to much aligned grain orientation (perpendicular to the contact surface) in the coating by APS (Fig. 5(d′ & f′)). Although the entire powder was melted and flattened from a sphere shape into a 2D lamellar after cooling down, each powder's grains were well indexed by EBSD. Nevertheless, there are still non-indexed areas mainly located at (1) the interface between the first layer of deposit and the substrate and (2) boundaries between lamellars. The impact between the molten droplets from the first pass and relatively cool and hard substrate causes the fragmentation at the contact surfaces, e.g., bottom of the first layer of molten droplets and top of the substrate. The grain sizes at this contact surfaces were believed to less than the minimum step size of 0.2 μm used in current EBSD. Hence, the interface was unindexed and appeared black under EBSD. At the subsequent pass, the fragmentation was less significant as the preceding deposit was still hot and soft. Therefore, only the boundaries between lamellars were un-indexed and possibly attributed to the presence of surface oxides.

V. Conclusion

In this work, Inconel 718 coatings deposited by cold spray (CS) using PG 718 powders were compared with the Inconel 718 coatings deposited by atmospheric plasm spray (APS) using Amdry 718 powders with optimized parameters for each spray technique, to illustrate the characteristics of each technique. CS mainly relies on the kinetic energies of the impacting softened powders to undergo plastic deformation and subsequently adhere to the substrate surface as a dense coating, while APS relies on solidification of the molten powders into a coating. As a result, the Inconel 718 coating's morphology, composition and crystallinity were similar to that the starting PG 718 powders. In addition, the forceful and successive impact causes grain fragmentation, presence of compressive residual stress (-30.5 ± 12.5 MPa) and much higher hardness (510.4 - 527.3 HV_{200g}, 8.2 GPa) in the Inconel 718 coating by CS, which was dense (0.2 - 0.5 %) but very brittle. On the other hand, APS produced a more porous Inconel 718 coating (0.8 - 1.5%) and similar crystallinity with the initial powders but higher O wt%. Solidification of the molten impacting powders led to aligned grains in the lamellar perpendicular to the contact surface, presence of tensile residual stress (254.4 ± 33.3 MPa) and lower hardness (227.5 – 252.2 HV_{200g}, 3.9 GPa). Adhesion strength from APS (76.4 ± 6.1 MPa) is slightly better than that from CS (74.0 ± 12.1 MPa), while the tensile strength, and ductility were much better than those by CS. Nevertheless, solution heat treatment has been reported able to reduce the compressive residual stress/hardness and improve the ductility of the Inconel 718 coatings deposited by CS. Therefore, in view that CS can produce dense and adherent Inconel 718 coatings, it is a promising alternative to APS or HVOF as a repairing technology for Inconel 718 components.

- **Author Information**

Corresponding Author:

*Tel.: +65-64197404

*Fax: +65-68720785

*E-mail address: pkaw@simtech.a-star.edu.sg

#Tel.: +65-63194919

#Fax: +65-68720785

#E-mail address: js-pan@imre.a-star.edu.sg

- **Acknowledgment**

This research is supported by the Agency for Science, Technology and Research (A*STAR) under its Singapore Aerospace Program (A1715a0073), and partially under Machining Learning Assisted Control of Metal Cold Spray and Shot Peening Processes (A1894a0032) and Structural Metal Alloy Program (A18b1B0061). The authors would like to thank Ms. Doreen LAI Mei Ying who has retired from IMRE for part of the EBSD analysis, and thank Mr. TAN Boon Hee and Mr. LOI Qizhong from Advanced Remanufacturing and Technology Centre (ARTC) for assistance with cold spray.

- **Data availability**

All the raw/processed data required to reproduce these findings can be made available from the corresponding author upon reasonable request.

- **References**

[1] T.M. Pollock, S. Tin, Nickel-based superalloys for advanced turbine engines: Chemistry, microstructure, and properties, J. Propul. Power, 22 (2006) 361-374.
[2] H. Qi, Review of INCONEL 718 Alloy: Its History, Properties, Processing and Developing Substitutes, Journal of Materials Engineering, 2 (2012) 92-100.
[3] E. Akca, A. Gursel, A Review on Superalloys and IN718 Nickel-Based INCONEL Superalloy,

Periodicals of Engineering and Natural Sciences, 3 (2015) 15-27.
[4] T. Petrat, B. Graf, A. Gumenyuk, M. Rethmeier, Laser Metal Deposition as Repair Technology for a Gas Turbine Burner Made of Inconel 718, Physics Procedia, 83 (2016) 761-768.
[5] C.S. Ramesh, D.S. Devaraj, R. Keshavamurthy, B.R. Sridhar, Slurry erosive wear behaviour of thermally sprayed Inconel-718 coatings by APS process, Wear, 271 (2011) 1365-1371.
[6] C. Lyphout, P. Nylen, L. Ostergren, Relationships Between Process Parameters, Microstructure, and Adhesion Strength of HVOF Sprayed IN718 Coatings, J. Therm. Spray Technol., 20 (2011) 76-82.
[7] C. Lyphout, P. Nylen, L.G. Ostergren, Adhesion Strength of HVOF Sprayed IN718 Coatings, J. Therm. Spray Technol., 21 (2012) 86-95.
[8] C. Lyphout, A. Fasth, P. Nylen, Mechanical Property of HVOF Inconel 718 Coating for Aeronautic Repair, J. Therm. Spray Technol., 23 (2014) 380-388.
[9] D. Levasseur, S. Yue, M. Brochu, Pressureless sintering of cold sprayed Inconel 718 deposit, Mater. Sci. Eng., A, 556 (2012) 343-350.
[10] W. Wong, E. Irissou, P. Vo, M. Sone, F. Bernier, J.G. Legoux, H. Fukanuma, S. Yue, Cold Spray Forming of Inconel 718, J. Therm. Spray Technol., 22 (2013) 413-421.
[11] R. Singh, K.H. Rauwald, E. Wessel, G. Mauer, S. Schruefer, A. Barth, S. Wilson, R. Vassen, Effects of substrate roughness and spray-angle on deposition behavior of cold-sprayed Inconel 718, Surf. Coat. Technol., 319 (2017) 249-259.
[12] R. Singh, S. Schruefer, S. Wilson, J. Gibmeier, R. Vassen, Influence of coating thickness on residual stress and adhesion-strength of cold-sprayed Inconel 718 coatings, Surf. Coat. Technol., 350 (2018) 64-73.
[13] S. Bagherifard, G. Roscioli, M.V. Zuccoli, M. Hadi, G. D'Elia, A.G. Demir, B. Previtali, J. Kondás, M. Guagliano, Cold spray deposition of freestanding Inconel samples and comparative analysis with selective laser melting, J. Therm. Spray Technol., 26 (2017) 1517-1526.
[14] W.H. Ma, Y.C. Xie, C.Y. Chen, H. Fukanuma, J. Wang, Z.M. Ren, R.Z. Huang, Microstructural and mechanical properties of high-performance Inconel 718 alloy by cold spraying, J. Alloys Compd., 792 (2019) 456-467.
[15] L.I. Perez-Andrade, F. Gartner, M. Villa-Vidaller, T. Klassen, J. Munoz-Saldana, J.M. Alvarado-Orozco, Optimization of Inconel 718 thick deposits by cold spray processing and annealing, Surf. Coat. Technol., 378 (2019) 124997.
[16] J. Fiebig, E. Bakan, T. Kalfhaus, G. Mauer, O. Guillon, R. Vassen, Thermal Spray Processes for the Repair of Gas Turbine Components, Adv. Eng. Mater., (2020) 1901237.
[17] R. Vaßen, J. Fiebig, T. Kalfhaus, J. Gibmeier, A. Kostka, S. Schrüfer, Correlation of Microstructure and Properties of Cold Gas Sprayed INCONEL 718 Coatings, J. Therm. Spray Technol., (2020).
[18] W. Sun, A.W.Y. Tan, A. Bhowmik, I. Marinescu, X. Song, W. Zhai, F. Li, E. Liu, Deposition characteristics of cold sprayed Inconel 718 particles on Inconel 718 substrates with different surface conditions, Materials Science and Engineering: A, 720 (2018) 75-84.
[19] W. Sun, A. Bhowmik, A.W.-Y. Tan, R. Li, F. Xue, I. Marinescu, E. Liu, Improving microstructural and mechanical characteristics of cold-sprayed Inconel 718 deposits via local induction heat treatment, J. Alloys Compd., 797 (2019) 1268-1279.
[20] W. Sun, A.W.-Y. Tan, A. Bhowmik, F. Xue, I. Marinescu, E. Liu, Evaluation of cold sprayed graphene nanoplates–Inconel 718 composite coatings, Surf. Coat. Technol., 378 (2019) 125065.
[21] D.D. Gu, W. Meiners, K. Wissenbach, R. Poprawe, Laser additive manufacturing of metallic components: materials, processes and mechanisms, Int. Mater. Rev., 57 (2012) 133-164.

[22] T. Schmidt, F. Gärtner, H. Assadi, H. Kreye, Development of a generalized parameter window for cold spray deposition, Acta Mater., 54 (2006) 729-742.
[23] Q. Wang, M.X. Zhang, Review on Recent Research and Development of Cold Spray Technologies, Key Eng. Mater., 533 (2013) 1-52.
[24] T. Stoltenhoff, C. Borchers, F. Gärtner, H. Kreye, Microstructures and key properties of cold-sprayed and thermally sprayed copper coatings, Surf. Coat. Technol., 200 (2006) 4947-4960.
[25] T. Hussain, D.G. McCartney, P.H. Shipway, D. Zhang, Bonding Mechanisms in Cold Spraying: The Contributions of Metallurgical and Mechanical Components, J. Therm. Spray Technol., 18 (2009) 364-379.
[26] M.R. Rokni, C.A. Widener, S.P. Ahrenkiel, B.K. Jasthi, V.R. Champagne, Annealing behaviour of 6061 aluminium deposited by high pressure cold spray, Surf. Eng., 30 (2014) 361-368.
[27] Y.M. Xiong, W.M. Zhuang, M.X. Zhang, Effect of the thickness of cold sprayed aluminium alloy coating on the adhesive bond strength with an aluminium alloy substrate, Surf. Coat. Technol., 270 (2015) 259-265.
[28] S. Rech, A. Trentin, S. Vezzù, E. Vedelago, J.-G. Legoux, E. Irissou, Different cold spray deposition strategies: Single- and multi-layers to repair aluminium alloy components, J. Therm. Spray Technol., 23 (2014) 1237-1250.
[29] X.J. Ning, J.H. Jang, H.J. Kim, C.J. Li, C. Lee, Cold spraying of Al-Sn binary alloy: Coating characteristics and particle bonding features, Surf. Coat. Technol., 202 (2008) 1681-1687.
[30] W. Wong, E. Irissou, A.N. Ryabinin, J.-G. Legoux, S. Yue, Influence of helium and nitrogen gases on the properties of cold gas dynamic sprayed pure titanium coatings, J. Therm. Spray Technol., 20 (2011) 213-226.
[31] W.Y. Li, C. Zhang, X.P. Guo, J.L. Xu, C.J. Li, H.L. Liao, C. Cocidet, K.A. Khor, Ti and Ti-6Al-4V coatings by cold spraying and microstructure modification by heat treatment, Adv. Eng. Mater., 9 (2007) 418-423.
[32] A.W.-Y. Tan, W. Sun, Y.P. Phang, M. Dai, I. Marinescu, Z. Dong, E. Liu, Effects of traverse scanning speed of spray nozzle on the microstructure and mechanical properties of cold-sprayed Ti6Al4V coatings, J. Therm. Spray Technol., 26 (2017) 1484-1497.
[33] Y. Zou, W. Qin, E. Irissou, J.-G. Legoux, S. Yue, J.A. Szpunar, Dynamic recrystallization in the particle/particle interfacial region of cold-sprayed nickel coating: Electron backscatter diffraction characterization, Scr. Mater., 61 (2009) 899-902.
[34] C.J. Huang, X.C. Yan, C.Y. Chen, Y.C. Xie, M. Liu, M. Kuang, H.L. Liao, Additive manufacturing hybrid Ni/Ti-6Al-4V structural component via selective laser melting and cold spraying, Vacuum, 151 (2018) 275-282.
[35] W. Sun, A.W.-Y. Tan, D.J.Y. King, N.W. Khun, A. Bhowmik, I. Marinescu, E. Liu, Tribological behavior of cold sprayed Inconel 718 coatings at room and elevated temperatures, Surf. Coat. Technol., 385 (2020) 125386.
[36] R.B. Heimann, Plasma-Spray Coating: Principles and Applications, Wiley-VCH Verlag GmbH, New York, 2007.
[37] E.F. Rauch, L. Dupuy, Rapid spot diffraction patterns identification through template matching, Arch. Metall. Mater., 50 (2005) 87-99.
[38] P. Moeck, S. Rouvimov, E.F. Rauch, M. Veron, H. Kirmse, I. Hausler, W. Neumann, D. Bultreys, Y. Maniette, S. Nicolopoulos, High spatial resolution semi-automatic crystallite orientation and phase mapping of nanocrystals in transmission electron microscopes, Cryst. Res. Technol., 46 (2011) 589-606.

[39] E.F. Rauch, M. Veron, Automated crystal orientation and phase mapping in TEM, Mater. Charact., 98 (2014) 1-9.
[40] Z. Zhang, M. Lin, D.H.L. Seng, S.L. Teo, F. Wei, H.R. Tan, A.K.H. Cheong, S.H. Lim, S. Wang, J. Pan, Fatigue Life Enhancement in Alpha/Beta Ti-6Al-4V after Shot Peening: An EBSD and TEM Crystallographic Orientation Mapping Study of Surface Layer, Materialia, (2020) 100813.
[41] C. Borchers, F. Gärtner, T. Stoltenhoff, H. Assadi, H. Kreye, Microstructural and macroscopic properties of cold sprayed copper coatings, J. Appl. Phys., 93 (2003) 10064-10070.
[42] B. Derby, The dependence of grain size on stress during dynamic recrystallisation, Acta Metall. Mater., 39 (1991) 955-962.
[43] C. Lee, J. Kim, Microstructure of Kinetic Spray Coatings: A Review, J. Therm. Spray Technol., 24 (2015) 592-610.
[44] T.W. Clyne, S.C. Gill, Residual Stresses in Thermal Spray Coatings and Their Effect on Interfacial Adhesion: A Review of Recent Work, J. Therm. Spray Technol., 5 (1996) 401.